

The energy flux spectrum of internal waves generated by turbulent convection

By Louis-Alexandre Couston^{1†}, Daniel Lecoanet², Benjamin Favier¹,
Michael Le Bars¹

¹ CNRS, Aix Marseille Univ, Centrale Marseille, IRPHE, Marseille, France

² Princeton Center for Theoretical Science, Princeton, NJ 08544, USA

(15 August 2018)

We present three-dimensional direct numerical simulations of internal waves excited by turbulent convection in a self-consistent, Boussinesq and Cartesian model of convective–stably-stratified fluids. We demonstrate that in the limit of large Rayleigh number ($Ra \in [4 \times 10^7, 10^9]$) and large stratification (Brunt-Väisälä frequencies $f_N \gg f_c$, where f_c is the convective frequency), simulations are in good agreement with a theory that assumes waves are generated by Reynolds stresses due to eddies in the turbulent region (Lecoanet & Quataert 2013). Specifically, we demonstrate that the wave energy flux spectrum scales like $k_{\perp}^4 f^{-13/2}$ for weakly-damped waves (with k_{\perp} and f the waves' horizontal wavenumbers and frequencies), and that the total wave energy flux decays with z , the distance from the convective region, like $z^{-13/8}$.

1. Introduction

Internal gravity waves can be found in planetary atmospheres and oceans, radiative envelopes of stars, and planetary fluid cores. Numerous studies have shown that internal gravity waves can drive strong large-scale flows (Grisouard & Bühler 2012; Bordes *et al.* 2012; van den Bremer & Sutherland 2018; Couston *et al.* 2018) and enhance turbulence and mixing (Staquet *et al.* 2002; Kunze 2017; Thorpe 2018). Through their effects on mean flows and properties of the fluid in which they propagate, internal waves can have a significant impact on the long-term evolution of global systems, such as Earth's climate (Alexander *et al.* 2010) or the differential rotation of stars (Rogers *et al.* 2012).

The energy flux of internal waves is required to accurately predict the influence of waves on global dynamics, but is difficult to estimate, especially when the generating source is turbulent. Nevertheless, turbulent sources account for a significant fraction of the internal wave energy in the atmosphere, stars and planetary interiors, so they can hardly be neglected. Turbulent motions in the bottom Ekman layer (Taylor & Sarkar 2007) or the surface mixed layer of the ocean (Munroe & Sutherland 2014), turbulent buoyant plumes in the atmosphere (Ansong & Sutherland 2010), fingering convection (Garaud 2018) and penetrative convection in stars (Pinçon *et al.* 2016) are examples of turbulent sources that can generate internal gravity waves.

Past studies of turbulence-driven internal waves have focused on extracting scaling laws for the total wave flux with respect to problem parameters. Information on the energy flux spectrum, i.e. the distribution of energy for different wavenumbers k and frequencies f of internal waves, is often beyond reach or difficult to interpret because of experimental or numerical constraints. For instance, the simulations of Rogers *et al.* (2013) were restricted to only 2D because of this difficulty. However, knowledge of the

† louisalexandre.couston@gmail.com

energy flux spectrum is essential to predicting wave effects, since both wave propagation, damping and interaction with the background state depend strongly on k and f .

Several theoretical approaches have been put forward to predict the wave spectrum due to turbulent motions. Under the linearized rapid distortion theory (e.g. Carruthers & Hunt 1986), the wave amplitude is proportional to the convective velocity. We instead assume the wave amplitude is linearly proportional to the Reynolds stress (i.e., the square of the convective velocity), which can accurately predict waves in direct numerical simulations (DNS) (Lecoanet *et al.* 2015). Two theoretical descriptions of the Reynolds stresses in turbulent convection are the “eddy” and “plume” theories. In the “eddy” theory, the convection is decomposed into eddies which follow Kolmogorov statistics and eddy stresses are used as generating sources of internal waves in the stable region (Goldreich & Kumar 1990; Lecoanet & Quataert 2013). In the “plume” theory, the convection is seen as an ensemble of uncorrelated plumes impinging at the base of the stable layer (Pinçon *et al.* 2016). The “plume” theory predicts the wave energy flux spectrum to be Gaussian in k and f ; the “eddy” theory predicts power laws.

Here we validate for the first time the prediction of the wave flux spectrum based on the “eddy” theory in the limit of strong stable stratification (Lecoanet & Quataert 2013) using 3D state-of-the-art DNS of a convective–stably-stratified fluid model. The DNS and analyses are challenging as they require a fully turbulent flow interacting with a strongly stratified layer and high spatial/temporal resolution to construct the spectra.

2. DNS model

The fluid model we use is similar to the one used in Couston *et al.* (2017), though here it is 3D (figure 1). We solve the Navier-Stokes equations under the Boussinesq approximation, i.e. the fluid density is $\rho = \rho_0 + \delta\rho$ with ρ_0 the (constant) reference density and $\delta\rho \ll \rho_0$ are small variations due to temperature fluctuations. We consider constant kinematic viscosity ν , acceleration due to gravity g and thermal diffusivity κ . The governing equations for the velocity $\mathbf{u} = (u, v, w)$ and temperature T in a Cartesian (x, y, z) frame of reference (\hat{z} is the upward-pointing unit vector of the z -axis) read

$$\partial_t \mathbf{u} + (\mathbf{u} \cdot \nabla) \mathbf{u} = -\nabla p + \nu \nabla^2 \mathbf{u} - g \delta\rho / \rho_0 \hat{z} - \mathbf{u} / \tau, \quad (2.1a)$$

$$\partial_t T + (\mathbf{u} \cdot \nabla) T = \kappa \nabla^2 T, \quad (2.1b)$$

$$\nabla \cdot \mathbf{u} = 0, \quad (2.1c)$$

with p the pressure and $-\mathbf{u} / \tau$ is a damping term used to prevent wave reflection from the top boundary. The density anomaly $\delta\rho$ is related to T through the equation of state

$$\delta\rho / \rho_0 = -\alpha(T)(T - T_i) = -\alpha_s(T - T_i)H(T - T_i) + \alpha_s \mathcal{S}(T - T_i)H(T_i - T), \quad (2.2)$$

with H the Heaviside function; $\alpha_s > 0$ is the thermal expansion coefficient for $T > T_i$, with T_i the inversion temperature at which the density anomaly $\delta\rho / \rho_0 = 0$ is maximum, and $\mathcal{S} > 0$ is the stiffness parameter. We assume periodicity in the horizontal directions and impose free-slip and fixed temperatures conditions on the top ($T = T_t$) and bottom boundaries ($T = T_b$), with $T_b > T_i > T_t$. Then, because equation (2.2) is nonmonotonic, the lower part of the fluid is convectively unstable, the upper part is stably stratified and \mathcal{S} indicates how sharp or “stiff” the transition is at the interface (Couston *et al.* 2017).

We use the characteristic length scale H , the thermal diffusion time H^2 / κ , and the temperature difference $\Delta T = T_b - T_i$ in order to define the non-dimensional variables:

$$(\tilde{x}, \tilde{y}, \tilde{z}) = \frac{(x, y, z)}{H}, \quad \tilde{t} = \frac{t\kappa}{H^2}, \quad \tilde{\mathbf{u}} = \frac{\mathbf{u}H}{\kappa}, \quad \tilde{T} = \frac{T - T_i}{\Delta T}, \quad \tilde{p} = \frac{pH^2}{\kappa^2}, \quad \tilde{\rho} = \frac{\delta\rho}{\rho_0\alpha_s\Delta T}. \quad (2.3)$$

Substituting (2.3) in (2.1)-(2.2) and dropping tildes we obtain the dimensionless equations

$$\partial_t \mathbf{u} + (\mathbf{u} \cdot \nabla) \mathbf{u} = -\nabla p + Pr \nabla^2 \mathbf{u} - Pr Ra \rho \hat{z} - \mathbf{u}/\tau, \quad (2.4a)$$

$$\partial_t T + (\mathbf{u} \cdot \nabla) T = \nabla^2 T, \quad (2.4b)$$

$$\nabla \cdot \mathbf{u} = 0, \quad (2.4c)$$

$$\rho = -TH(T) + \mathcal{S}TH(-T), \quad (2.4d)$$

with $Pr = \nu/\kappa$ the Prandtl number and $Ra = \alpha_s g \Delta T H^3 / (\nu \kappa)$ the Rayleigh number. We note L_x, L_y, L_z the dimensionless lengths of the domain in x, y, z directions and $T_{top} < 0$ the dimensionless temperature at $z = L_z$ ($T = 1$ at $z = 0$ and the inversion temperature is $T = 0$ in dimensionless space). The dimensionless z -dependent damping coefficient used to prevent wave reflection from the top boundary is $\tau^{-1}(z) = 0.5 f_{N^*} \{\tanh[(z - L_z + 0.15)/0.05] + 1\}$ with f_{N^*} the target buoyancy frequency (cf. next section).

We solve (2.4) using the open-source pseudo-spectral code DEDALUS (Burns *et al.* 2018). We are interested in DNS results at statistical steady-state and in the limit of fully turbulent convection (large Ra) and strong stable stratification (large \mathcal{S}). For ease of presentation, we want the convection to extend from $z = 0$ to $z = h \approx 1$ at thermal equilibrium, i.e. such that H is approximately the size of the convection zone in dimensional variables and Ra is the effective Rayleigh number of the convection. h is an output of our simulations, but it can be controlled by iteratively adjusting T_{top} (all other parameters fixed). At leading order, $h \approx 1$ when T_{top} is chosen such that the measured heat flux $Q = \overline{wT} - \overline{T_z}$ in the convection (overbar denotes the horizontal average) equals the expected diffusive heat flux of the stable region $\sim -T_{top}/(L_z - h)$ with $h = 1$. Because Q in the convection zone changes with T_{top} , finding T_{top} is carried out iteratively. We fix all problem parameters except T_{top} , make an initial guess for T_{top} , and run a simulation for a few convective turnover times, initialized with a temperature of $T = (1 - z)H(1 - z) + T_{top}(z - 1)H(z - 1)$ plus low-amplitude noise. We then update our guess for T_{top} using $T_{top} = -Q(L_z - h)$ with $h = 1$, where Q is the average heat flux at $z = 0$, and we reiterate until T_{top} doesn't change by more than about 10%. The final T_{top} gives an estimate for the buoyancy frequency $f_{N^*} = \sqrt{-Pr Ra \mathcal{S} T_{top} / (L_z - 1)} / (2\pi)$ used in the expression for the damping term τ in (2.4a). The actual buoyancy frequency $f_N = N / (2\pi)$ is computed using $N = \sqrt{Pr Ra \mathcal{S} Q}$ with Q averaged from $z = 0$ to $z = 1$ and over the simulation time Δt . In all the simulations, we set $L_x = L_y = L_z = L$ with $L = 2$ or $L = 3$. Therefore, the ratio between the horizontal and vertical extent of the convective zone is larger than 2, which ensures that confinement effects associated with the horizontal periodic boundary conditions are not dominating the dynamics. We set $Pr = 1$ for simplicity. Input and output parameters of the eight simulations included in this paper are reported in table 1.

The variables of interest include the kinetic energy spectrum and the energy flux spectrum. The kinetic energy per unit surface area and unit (thermal) time reads

$$K(z) = \int \frac{|\mathbf{u}|^2 dx dy dt}{2 L^2 \Delta t} \approx \sum_{f_i, k_{\perp j}} \frac{|\hat{\mathbf{u}}|^2}{2 \delta f \delta k_{\perp}} \delta f \delta k_{\perp} \equiv \sum_{f_i, k_{\perp j}} dK \delta f \delta k_{\perp} \approx \int \frac{\partial^2 K}{\partial f \partial k_{\perp}} df dk_{\perp}, \quad (2.5)$$

with hat denoting the Fourier transform in (x, y, t) , Δt the period over which results are integrated in time, k_{\perp} and f are the horizontal wavenumber and frequency, δk_{\perp} and δf are the unit increments in spectral space, and dK is the discrete version of the kinetic

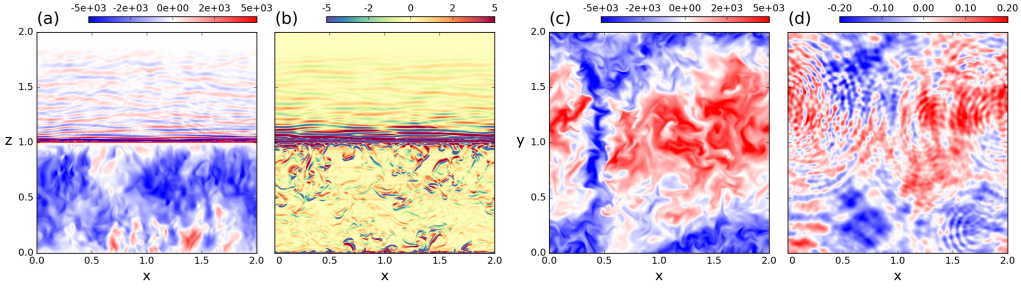


FIGURE 1. Snapshots of (a) $w(y = 0)$, (b) $T_z - \overline{T}_z$ at $y = 0$ (overbar denotes x average), (c) $w(z = 0.7)$, (d) $w(z = 1.3)$ for case C_8^{400} . Variables in the wave region ($z > 1$) in (a), (b) have been multiplied by 10^4 , 10^3 , respectively. A movie is available as Supplementary Material.

Name	$\frac{Ra}{10^8}$	S	T_{top}	L	$n_x n_y \times (n_{zl} + n_{zu})$	$\frac{\delta t}{10^{-7}}$	$\frac{f_c}{10^3}$	$f_c \Delta t$	$\frac{f_c}{u_{rms}}$	$\frac{f_N}{f_c}$
C_7^{10}	0.4	10	-86	3	$256^2 \times (384 + 256)$	0.5	1.1	9.8	1.6	19
C_7^{100}	0.4	100	-35	2	$256^2 \times (384 + 128)$	2	1.2	10	1.5	50
C_7^{400}	0.4	400	-32	2	$256^2 \times (384 + 192)$	2	1.3	10.7	1.9	86
C_8^{10}	2	10	-140	3	$256^2 \times (512 + 256)$	0.2	2.6	7.1	1.6	23
C_8^{50}	2	50	-62	2	$256^2 \times (512 + 256)$	0.6	2.5	9.1	1.5	49
C_8^{100}	2	100	-60	2	$256^2 \times (512 + 256)$	0.6	2.4	12.5	1.4	71
C_8^{400}	2	400	-52	2	$512^2 \times (768 + 384)$	0.6	3.0	3.8	1.9	109
C_9^{100}	10	100	-100	2	$512^2 \times (768 + 256)$	0.1	5.4	5.4	1.7	90

TABLE 1. Simulation parameters: number of Fourier modes n_x, n_y in x, y directions, Chebyshev modes n_{zl}/n_{zu} in lower/upper regions of the compound z basis (stitched at $z = 1.2$), typical time steps δt , best-fit convective frequency f_c for $\mathcal{A} = 30$ (cf. §4.2), time $f_c \Delta t$ of data collection, convective velocity u_{rms} and Brunt-Väisälä frequency f_N . $Pr = 1$ for simplicity.

energy spectrum $\frac{\partial^2 K}{\partial f \partial k_\perp}$. Similarly, we define the z -dependent vertical energy flux as

$$F(z) = \int wp \frac{dx dy dt}{L^2 \Delta t} \approx \sum_{f_i, k_\perp j} \frac{\mathcal{R}(\hat{w} \hat{p}^*)}{\delta f \delta k_\perp} \delta f \delta k_\perp \equiv \sum_{f_i, k_\perp j} dF \delta f \delta k_\perp \approx \int \frac{\partial^2 F}{\partial f \partial k_\perp} df dk_\perp, \quad (2.6)$$

where $*$ denotes the complex conjugate, dF is the discrete energy flux spectrum and \mathcal{R} denotes the real part. Note that throughout this paper, we assume isotropic motions in x, y directions and express variables in spectral space in terms of the average horizontal wavenumber $k_\perp = (k_x^2 + k_y^2)^{1/2}$ (with k_x, k_y the wavenumbers in x, y directions). Thus, $|\hat{u}|^2 \equiv |\hat{u}(k_\perp)|^2$ is the azimuthal average of $|\hat{u}(k_x, k_y)|^2$ and $\mathcal{R}(\hat{w} \hat{p}^*)$ is the azimuthal average of $\mathcal{R}[\hat{w}(k_x, k_y) \hat{p}^*(k_x, k_y)]$ based on the modulus of vector (k_x, k_y) , i.e. averaging over all orientations. We apply a Hann windowing function to all variables before taking the time Fourier transform and we discard the modes $f = 0$ and $k_\perp = 0$ from the spectra.

3. Theoretical prediction

We now describe a heuristic model which predicts the wave energy flux spectrum at the interface, $F^i(f, k_\perp)$, between the convective and stably-stratified layers. This is based on the calculation in Lecoanet & Quataert (2013) (specifically, the “discontinuous” N^2 case), which itself is based on the earlier calculation in Goldreich & Kumar (1990). We

first assume that turbulence driven by the convection can be decomposed into “eddies,” each of which has a characteristic length h and velocity u_h . The largest such “eddy” is the large-scale circulation of the convection, which has length $\ell_c = 2\pi/k_c$ and velocity u_c . We imagine this large scale circulation represents the injection scale of a Kolmogorov turbulent cascade and to recover the $k^{-5/3}$ energy spectrum (k is the three-dimensional wavenumber), we require that the typical velocity of eddies with size h scales like $u_h/u_c = (h/\ell_c)^{1/3}$. We assume each eddy is coherent for an eddy turnover time $\tau_h = h/u_h$, which implies that the power spectrum in the convection zone is peaked along the curve $\tau_h f_c = (h/\ell_c)^{2/3}$. This ignores the fact that small eddies can be advected over their size h on timescales shorter than τ_h by large-scale motions. This set of assumptions is very simplistic, but allows a theoretical derivation of the wave energy flux spectrum.

In this hypothesis, the waves are generated by Reynolds stresses within the convection zone. We calculate the waves generated by a single eddy with size h and corresponding turnover time τ_h , and then sum up the wave energy flux over all eddies. An eddy with size h and turnover time τ_h can only efficiently excite a wave with frequency f and wavenumber k_\perp if both

$$f \leq \tau_h^{-1}, \quad \ell_c(k_\perp/2\pi) \leq \ell_c/h = (\tau_h f_c)^{-3/2}. \quad (3.1)$$

This is because we assume the spectral representation of an eddy’s velocity field is peaked at wavenumbers around $2\pi/h$ and decreases exponentially at higher wavenumbers due to analyticity (and similarly for the temporal spectrum with timescale τ_h). Waves with $f > \tau_h^{-1}$ or $k_\perp > 2\pi/h$ then have exponentially small coupling to eddies of size h .

To connect the properties of the convection to the waves, one can write an equation for the wave velocity as a function of turbulent stresses as (Lecoanet & Quataert 2013),

$$\nabla^2 \partial_t^2 w + N^2(z)(\partial_x^2 + \partial_y^2)w = S, \quad (3.2)$$

where S is related to the Reynolds stresses associated with convective eddies. Note that we have neglected the effects of diffusion in the excitation process. We also neglect thermal stresses within the convection zone (as in Lecoanet *et al.* 2015). Lecoanet & Quataert (2013) derives the internal waves’ Green’s function from this equation assuming $N^2(z)$ is constant in the convective and stably-stratified region, and discontinuous at the interface. One can then estimate the convolution of this Green’s function with the Reynolds stress of an eddy to find that the wave energy flux from eddies of size h is

$$\frac{dF^i}{d \log k_\perp d \log f d \log h} = \mathcal{A} u_h^3 \frac{f_c}{f_N} \frac{f}{f_c} \left(\frac{k_\perp h}{2\pi} \right)^4 = \mathcal{A} u_c^3 \frac{f_c}{f_N} \frac{f}{f_c} \frac{h}{\ell_c} \left(\frac{k_\perp h}{2\pi} \right)^4, \quad (3.3)$$

with \mathcal{A} a multiplicative constant, assumed universal, i.e. independent of all problem, wave or eddy parameters. To calculate the wave energy flux for a given frequency and wavenumber, we must sum up excitation from all eddies which satisfy equation (3.1). Because of the strong dependence on the eddy size in equation (3.3), the wave energy flux is dominated by the largest possible eddies which can excite a wave. The wave energy flux depends on whether the wave frequency is higher or lower than the frequency of the largest generating eddy $f^*(k_\perp) = f_c[\ell_c k_\perp/(2\pi)]^{2/3}$. Waves with (k_\perp, f) satisfying $f < f^*(k_\perp)$ are not observed in the bulk of the stable region in DNS because they are strongly dissipated (see discussion after (3.5)), so we neglect their contribution to the energy flux in the theory. The expression for the flux of the waves we keep, i.e. with frequency $f > f_c[\ell_c k_\perp/(2\pi)]^{2/3}$, is

$$\frac{dF^i}{d \log k_\perp d \log f} = \mathcal{A} u_c^3 \frac{f_c}{f_N} \left(\frac{f}{f_c} \right)^{-13/2} \left(\frac{k_\perp \ell_c}{2\pi} \right)^4. \quad (3.4)$$

We recall that equation (3.4) is a prediction for the energy flux spectrum of *inviscid propagating wave modes* at the convective–stably-stratified interface. In the DNS, however, the energy flux at the interface has contributions from both *inviscid and viscous wave modes* and overshooting *plumes*, such that it is not expected to match the prediction (3.4). In order to avoid this discrepancy, we compare the theory with DNS away from the interface, where overshooting plumes and strongly-viscous modes can be neglected.

In order to extend the expression for the flux (3.4) at the interface to an expression valid in all of the stable layer we derive a wave decay rate from the linear equation

$$(\partial_t - \nabla^2)^2 \nabla^2 w + N^2 (\partial_x^2 + \partial_y^2) w = 0, \quad (3.5)$$

valid for $Pr = 1$. Note this differs from the *inviscid* equation (3.2) used to derive the wave flux *at the interface*. Substituting a plane wave solution $w \sim e^{i(k_x x + k_y y - \omega t)} e^{i(k_z - \gamma)z}$ with $\omega > 0$ in (3.5) yields a cubic complex equation for $(ik_z - \gamma)^2$ whose six roots can be written in closed form. We assume that motions in the stable layer are dominated by waves propagating upward, i.e. with group velocity $C_{gz} = \partial\omega/\partial k_z > 0$, and whose amplitude decrease with z . One of the three roots (k_{zj}, γ_j) with $C_{gzj} > 0$ has a much smaller decay rate γ_j than the other two, such that it is expected to be the dominant contribution to upward-propagating and decaying waves in DNS. Unsurprisingly, this solution is the “full-dissipation” equivalent of the simpler WKB solution

$$k_z = \mp k_\perp N/\omega, \quad \gamma = \pm k_\perp^3 N^3/\omega^4, \quad (3.6)$$

with $k_z < 0$ for upward-propagating waves, derived in the weak dissipation limit and valid when $\omega \gg k^2 \geq O(1)$ and $\omega^2 \ll N^2$. We neglect the other two more-rapidly decaying upward-propagating wave solutions of (3.5). Note that whether they capture some of the turbulent energy is beyond the scope of this work, and neglecting them is consistent with prediction (3.4) since the theory only considers the WKB mode (3.6) in its inviscid form. Given that a broad range of frequencies and wavenumbers is excited in the DNS, it may be expected that (3.6) does not accurately predict the decay rate of the dominant waves. However, we find that the WKB solution and the “full-dissipation” solution for γ yield similar results for the theoretical spectra presented here, so for simplicity we will use (3.6) in the remainder of this paper (note that this suggests that the discrepancy between the “full” and the WKB decay rate is significant only when both decay rates are so large that it affects waves whose amplitudes are so small that they can be neglected). Note for future discussions that the decay rate is strongest for low-frequency high-wavenumber waves, as clearly shown by (3.6).

Finally, the z -dependent theoretical wave flux spectrum becomes

$$\frac{dF^{th}}{d \log k_\perp d \log f} = \frac{dF^i}{d \log k_\perp d \log f} e^{-2\gamma(z-z_i)} = \mathcal{A} u_c^3 \frac{2\pi f_c}{N} \left(\frac{f}{f_c}\right)^{-\frac{13}{2}} \left(\frac{k_\perp \ell_c}{2\pi}\right)^4 e^{-2\gamma(z-z_i)}, \quad (3.7)$$

with γ given by (3.6) and z_i the interface height. A useful approximate expression can be obtained for the total flux as a function of z by integrating (3.7) in the limit $f_N \gg f_c \gg (z - z_i) k_c^3/\pi$ and sufficiently far from the interface, i.e. $z - z_i \gg [\gamma(k_c, f_c)]^{-1}$. The derivation is tedious but straightforward, yielding (cf. Appendix A)

$$F^{th} = \int_{f_c}^{f_N} \int_{k_c}^{k_c(\frac{f}{f_c})^{\frac{3}{2}}} \frac{dF^{th}}{df dk_\perp} dk_\perp df \approx \mathcal{A} u_c^3 \frac{f_c^{\frac{15}{2}}}{f_N^{\frac{47}{8}}} \frac{5\Gamma(\frac{5}{8}) \ell_c^{\frac{39}{8}}}{28(8\pi^2)^{\frac{13}{8}}} (z - z_i)^{-\frac{13}{8}} \equiv \tilde{\mathcal{F}} (z - z_i)^{-\frac{13}{8}}. \quad (3.8)$$

The domain of validity of the asymptotic solution is expected to encompass all of the wave region in DNS. In the next section we show that the wave flux spectrum in DNS follows the trends predicted by the theory, i.e. equations (3.4) and (3.8).

4. Results and discussion

4.1. Statistics of turbulent convection

The theory described in section 3 assumes that the spatial correlations of the turbulent convection follow the standard Kolmogorov prediction for homogeneous and isotropic turbulence. Figure 2(a) shows that the frequency-integrated kinetic energy spectrum $\sum_{f_i} dK\delta f$ indeed has a slope relatively close to $k_{\perp}^{-5/3}$ for all simulations, thus validating the use of Kolmogorov hypothesis. The theory also requires prescription of the temporal correlations of the turbulence fluctuations. Here, the theory uses the eddy turnover time as the relevant time scale, which is known as the straining hypothesis. However, one could argue that the temporal correlations of small-scale turbulent features seen at a fixed point in space are affected by the advection by large-scale motions, and that the sweeping hypothesis should be considered instead (Tennekes 1975; Chen & Kraichnan 1989). The wavenumber integrated kinetic energy spectrum in 2(b) shows a frequency scaling somewhat weaker than $f^{5/3}$, which is the typical scaling for turbulent flows in Eulerian frame with sweeping (Chevillard *et al.* 2005; Canet *et al.* 2017), in agreement with convection experiments (Sano *et al.* 1989). The straining mechanism would instead lead to a steeper f^{-2} scaling, which is recovered when computing temporal correlations along Lagrangian trajectories in homogeneous turbulence (Chevillard *et al.* 2005) and in Rayleigh-Bénard convection (Liot *et al.* 2016). Figure 2(c) shows $k_{\perp}fdK$ for simulation C_9^{100} in (k_{\perp}, f) space, thus providing a more detailed picture of the turbulence statistics of the most turbulent simulation (similar results are obtained for other simulations). Again, it can be seen that the line of maximum $k_{\perp}fdK$ is reasonably well approximated by a power fit of the form $f \sim k_{\perp}^a$ (solid black line), with a close to 1 for all simulations, suggesting strong sweeping effects. Isocontours at higher frequencies, however, have a milder slope $f \sim k_{\perp}^b$ with $b < 1$, possibly suggesting that the eddy dominant frequency does scale like $\sim k_{\perp}^{2/3}$ (solid white line) and that sweeping does not affect all eddies. We will show that there is a good agreement between DNS results and the theory based on the straining hypothesis despite the presence of a strong large-scale flow. It should be noted that the theory in §3 changes with the choice of temporal correlations, as is already the case for other wave generation mechanisms by turbulence (for sound waves, see e.g. Zhou & Rubinstein 1996; Favier *et al.* 2010).

4.2. Integrated wave energy flux

In this section we compare the total energy flux $F(z)$ obtained in DNS with the theoretical prediction $F^{th}(z)$ (cf. (3.8)), and we infer the free parameters of the theory \mathcal{A} and f_c from a best fit. The theoretical total flux F^{th} has a steep scaling with the buoyancy frequency f_N , the interface height z_i and the turbulence parameters ℓ_c , f_c and u_c . While f_N and z_i are relatively well-constrained, the turbulence parameters are challenging to estimate from DNS of turbulent convection, making F^{th} potentially highly sensitive to the definitions used. A slight variation of f_c by a factor of 2, due to a change of definition, can lead to a change of F^{th} by a factor of ≈ 200 at all heights. Here, instead of estimating the values of the turbulence parameters using ad-hoc definitions, we use a best-fit approach. For simplicity, we assume that $\ell_c = 1$ in all cases and thus take $u_c = f_c$. This leaves f_c as the only free parameter in the theory, besides \mathcal{A} , which is assumed to be the same for all simulations. A posteriori, we check that the best-fit f_c is not too different from the

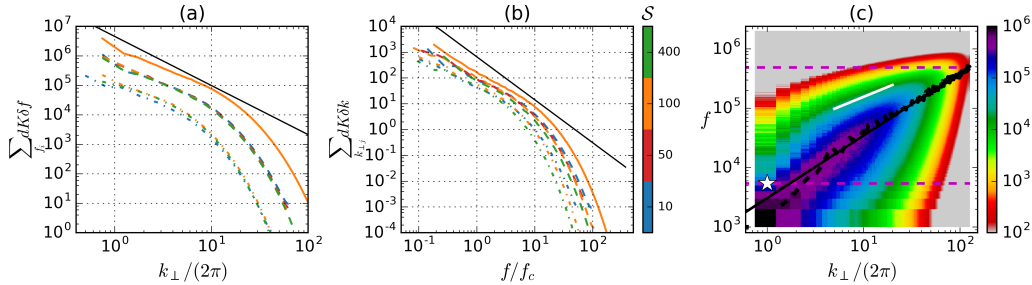


FIGURE 2. Integrated kinetic energy at $z = 0.7$ as a function of (a) k_{\perp} and (b) f . Solid, dash-dash, and dash-dot lines correspond to $Ra = 4 \times 10^7, 2 \times 10^8, 10^9$ and different colors correspond to different stiffnesses. Black solid lines are power laws with slope $-5/3$. (c) Kinetic energy spectrum $k_{\perp} f dK$ at $z = 0.7$ for C_9^{100} . The white star shows the wavenumber-frequency pair (ℓ_c^{-1}, f_c) of the large-scale circulation that allows a good agreement of the DNS with the theory. The pair (ℓ_c^{-1}, f_c) is not unreasonably far from the line $f(k_{\perp})$ of maximum energy, which is shown by the black dash-dash line (with solid line showing the linear fit). Dashed purple lines show f_c, f_N . The solid white line shows slope $+2/3$.

rms velocity $u_{rms} = \sqrt{2\mathcal{K}}$ at $z = 0.7$ in the convection zone (cf. equation (2.5) and note that u_{rms} is relatively depth-invariant in the convective bulk).

We obtain f_c for each simulation case by requiring that the asymptotic prediction for the total flux (3.8) equals the total flux in DNS at some height z^* in the wave region, i.e.

$$f_c^{\frac{21}{2}} = \frac{F(z^*)}{\mathcal{A}} f_N^{\frac{47}{8}} \frac{28(8\pi^2)^{\frac{13}{8}}}{5\Gamma(5/8)} (z^* - z_i)^{\frac{13}{8}}. \quad (4.1)$$

This definition of f_c may appear degenerate since f_c can take different values depending on \mathcal{A} or z^* . However, as discussed below (cf. also figure 3a), once \mathcal{A} is chosen, f_c does not depend on z^* provided that z^* is sufficiently far from the interface (i.e. $z^* > 1.1$). With $\mathcal{A} \sim \mathcal{O}(10)$, we find for all simulations that f_c is almost equal to u_{rms} (to within a factor of 2), which can be considered as a reference value for the turnover time of the largest-scale eddies (Lecoanet *et al.* 2015). From now on we will set the multiplicative constant arbitrarily to $\mathcal{A} = 30$. Other values could be chosen, but do not lead to significant changes as long as f_c is relatively close to u_{rms} .

We compare DNS results for $F(z)$ (symbols) with the theoretical prediction $F^{th}(z)$ (solid lines) in figure 3(a) for the eight simulation cases, using the parameter values listed in table 1 (i.e. with $\mathcal{A} = 30$). The total wave flux decreases with z in all cases and, as expected, is larger for higher Ra (for fixed \mathcal{S}) and lower \mathcal{S} (for fixed Ra) (Couston *et al.* 2017). With f_c obtained from a best-fit at just one particular height, we find an excellent agreement between DNS and the theoretical prediction in all of the bulk of the wave region ($z \in [1.1, 1.8]$) for all simulations, which demonstrates that f_c would be similar for any $z^* \in [1.1, 1.8]$. The $(z - 1)^{-13/8}$ scaling predicted by the asymptotic solution is well verified in figure 3(b), which shows the normalized wave flux F/\bar{F} (cf. equation (3.8)). All DNS results collapse on the asymptotic solution $(z - 1)^{-13/8}$ shown by the dashed line for $(z - 1) \in [0.1, 0.8]$, demonstrating that the theoretical flux spectrum integrated over the full range of waves excited compares well with the total flux in DNS.

4.3. Wave energy flux spectrum

We now investigate in details the scalings of the wave flux spectrum $k_{\perp} f dF$ in DNS with k_{\perp} and f , and discuss how they compare with the theoretical prediction $\sim k^4 f^{-13/2}$. We first show in figure 4(a)-(c) the overall wave flux spectrum $k_{\perp} f dF$ in (k, f) space at heights $z = 1, 1.1, 1.5$ for simulation C_9^{100} , which is the most turbulent case. The wave

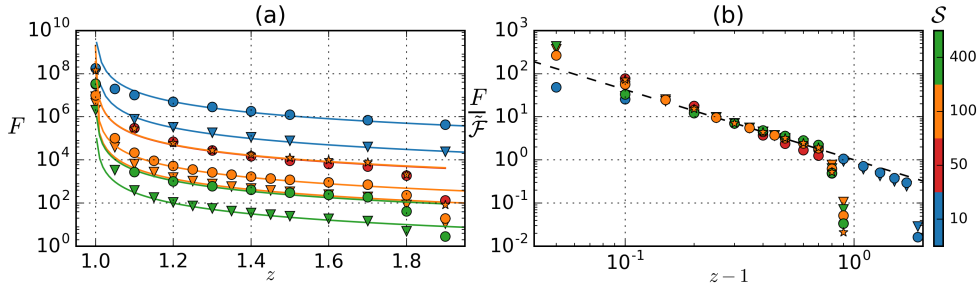


FIGURE 3. (a) Total flux in the wave region in DNS (triangles, circles, stars show results for $Ra = 4 \times 10^7, 2 \times 10^8, 10^9$) along with the predictions F^{th} (solid lines) using the best-fit values for \mathcal{A} and f_c reported in table 1. (b) The normalized flux F/\tilde{F} collapses for all simulations on the prediction $F^{th}/\tilde{F} \approx (z-1)^{-13/8}$ (dashed line) for $(z-1) \in [0.1, 0.8]$ (cf. Eqn (3.8)).

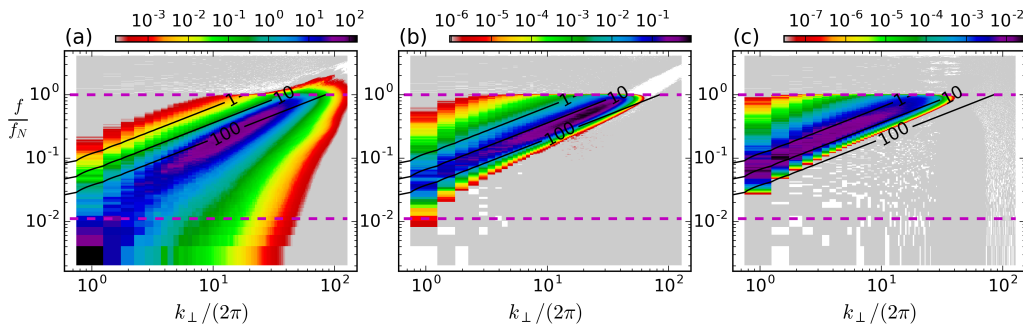


FIGURE 4. Wave flux spectrum $k_{\perp} f dF$ in DNS for case C_9^{100} at (a) $z = 1.0$, (b) 1.1, (c) 1.5. The color scale is shifted to lower amplitudes from (a) to (c) because the wave flux decreases with height. Solid black lines show isocontours of the decay rate 2γ . Dashed purple lines show f_c, f_N . White bins indicate $k_{\perp} f dF$ values that are negative.

flux at $z = 1$ can be difficult to interpret because it contains traces from both waves and overshooting plumes, with one or the other type dominating depending on whether the convection zone extends slightly above or slightly below $z = 1$. At $z = 1.1, 1.5$, however, we are clearly in the wave region and the spectrum has all of the features predicted by the theory: in the high-frequency low-wavenumber range (top left corner), the wave flux spectrum decreases rapidly with frequency and increases with wavenumber up to a cutoff wavenumber. The line of maximum wave flux spectrum overlaps with an isocontour of the decay rate 2γ (cf. solid black lines and equation (3.6)), and that isocontour is closer to the top left corner as z increases because this corner corresponds to waves which are the least damped. The wave flux spectrum falls off quickly at frequencies $f > f_N$ (top dashed line), which is the maximum frequency for propagating waves. Note that while upward-going waves require $dF > 0$, few (f, k_{\perp}) modes can be seen to have azimuthally-averaged $dF \leq 0$ in figures 4 (shown by white bins). However, they have negligible $|dF|$ compared to positive dF 's, which is why we restrict the colormap to $dF > 0$ only.

The wave flux spectrum is shown as a function of f for fixed wavenumber in figures 5(a),(b), and as a function of k_{\perp} for fixed frequency in figures 5(c),(d), providing a quantitative comparison of DNS results (solid lines) with the theory (dashed lines). The decrease of the wave flux spectrum in DNS with f is steep and close to the predicted $f^{-13/2}$ scaling (shown by the blue solid line). The increase of the wave flux spectrum with k_{\perp} closely follows the scaling k_{\perp}^4 , also predicted by the theory (shown by the blue solid line). Again, in figures 5(a),(b) [resp. (c),(d)] we note that the maximum flux moves

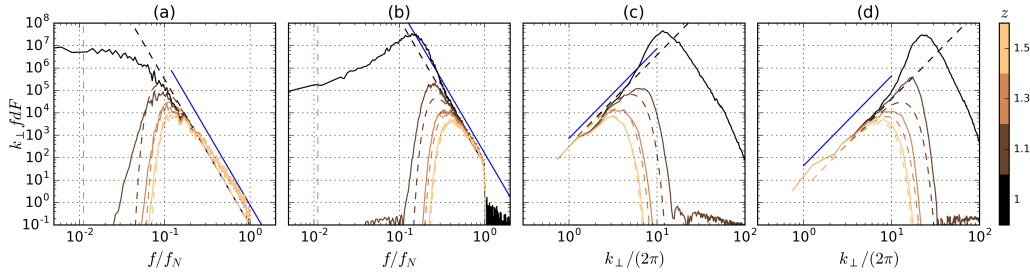


FIGURE 5. Wave flux spectrum $k_{\perp} f dF$ for fixed $k_{\perp}/(2\pi) = 1.7, 8.2$ [(a)-(b)] and fixed $f/f_N = 0.2, 0.4$ [(c)-(d)] for case C_9^{100} . Lighter colors show results at higher heights. Solid lines show DNS results and dashed lines show theoretical results using the convection parameters listed in table 1. The blue lines show the theoretical scalings.

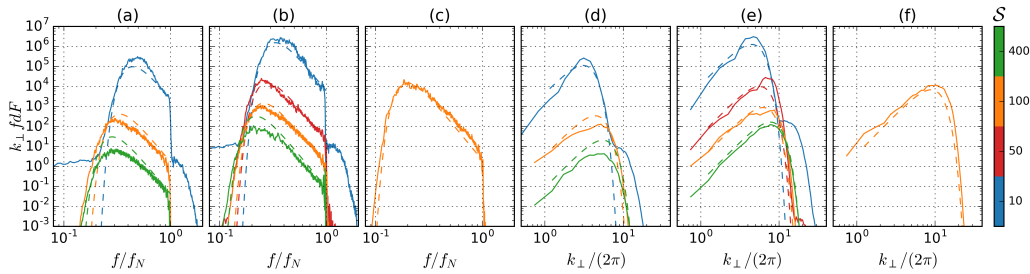


FIGURE 6. Wave flux spectrum $k_{\perp} f dF$ at $z = 1.3$ for fixed $k_{\perp}/(2\pi) = 3.7$ [(a)-(c)] and fixed $f/f_N = 0.4$ [(d)-(f)] with $Ra = 4 \times 10^7, 2 \times 10^8, 10^9$ increasing from (a) to (c) and (d) to (f). The different colors correspond to different stiffnesses \mathcal{S} . Solid lines show DNS results and dashed lines show theoretical results using the convection parameters listed in table 1.

toward higher frequencies (resp. lower wavenumbers) at higher z as a result of damping. We have checked that similar trends in frequency space and wavenumber space are obtained for other low wavenumbers (within the inertial subrange) and high frequencies ($f \gg u_{rms}$), suggesting an overall good agreement between DNS and theory for C_9^{100} .

We now demonstrate that a good agreement is obtained between DNS and the theory not only for C_9^{100} but for all simulations listed in table 1. In figures 6(a)-(c), we show the wave flux spectrum at $z = 1.3$ as a function of f for $k_{\perp} = 3.7$ with $Ra = 4 \times 10^7, 2 \times 10^8, 10^9$ in (a), (b), (c). Clearly, the DNS results (solid lines) overlap well with the theoretical predictions (dashed lines) obtained after estimating the convective frequency f_c from a best-fit approach (cf. §4.2 and listed values in table 1). A good agreement is similarly obtained for the wave flux spectrum at $z = 1.3$ as a function of k_{\perp} and for $f/f_N = 0.4$ between DNS and the theory (cf. figures 6(d)-(f)). We have checked that similar overlaps between DNS and theory are obtained for other fixed wavenumbers in the inertial subrange and frequencies $f_N > f \gg f_c$.

5. Concluding remarks

We have shown that the scaling of the energy flux spectrum of internal waves generated by turbulent convection in DNS follows the $k_{\perp}^4 f^{-13/2}$ prediction in the high $\mathcal{S} \gg 1$ regime (Lecoanet & Quataert 2013), and consistently, the total flux decreases as $(z - 1)^{-13/8}$ for all simulations presented. As discussed in the previous section, we can match the flux predicted by the theory to the DNS if we multiply the analytical prediction by a universal constant \mathcal{A} and use a best-fit for f_c . It is unsurprising that the theory needs to be rescaled since numerical factors have been dropped off along the derivation, and it is equally unsurprising that the best-fit f_c equals a few times the reference frequency based on the

rms velocity u_{rms} . It is worth pointing out, however, that there are some variations of f_c/u_{rms} across cases, which may mask some effects not included in the theory. Future work should explore the sweeping hypothesis, and include longer integration time with additional simulations or laboratory experiments in the high turbulence, high \mathcal{S} regime.

It is remarkable that there is such a satisfactory agreement between the DNS and an approximate-at-best theory based on second-order statistics of turbulent motions. The theory, as simple as it is, may prove useful in assessing the detectability of internal waves in geophysical and astrophysical fluids such as stars and in estimating wave-driven changes of global dynamics from the energy in turbulent sources.

Acknowledgements. The authors acknowledge funding by the European Research Council under the European Union's Horizon 2020 research and innovation program through Grant No. 681835-FLUDYCO-ERC-2015-CoG. D. L. is supported by a PCTS fellowship and a Lyman Spitzer Jr fellowship. Computations were conducted with support by the HPC resources of GENCI-IDRIS (Grant No. A0020407543 and A0040407543) and by the NASA High End Computing (HEC) Program through the NASA Advanced Supercomputing (NAS) Division at Ames Research Center on Pleiades with allocations GID s1647 and s1439.

Appendix A.

Here we present the key steps required to derive (3.8). Let us use the variables $f/f_c = \xi$, $k/k_c = \eta$, $2(2\pi)^2[k_c/(2\pi)]^3 f_N^3 f_c^{-4}(z - z_i) = z^*$. The integration of (3.8) in η results in

$$\begin{aligned} \frac{F(z)}{w_c^3 \frac{f_c}{f_N}} &= \int_1^{\frac{f_N}{f_c}} \int_1^{\xi^{\frac{3}{2}}} \frac{\xi^{-\frac{13}{2}} \eta^4}{\xi \eta} e^{-\eta^3 \xi^{-4} z^*} d\eta d\xi = \int_1^{\frac{f_N}{f_c}} \xi^{-\frac{15}{2}} \int_1^{\xi^{\frac{3}{2}}} \eta^3 e^{-\eta^3 \xi^{-4} z^*} d\eta d\xi \\ &= \int_1^{\frac{f_N}{f_c}} \left\{ \underbrace{\frac{1}{3z^*} \left[\xi^{-\frac{7}{2}} e^{-\xi^{-4} z^*} - \xi^{-2} e^{-\xi^{\frac{1}{2}} z^*} \right]}_{\mathcal{I}_1} + \underbrace{\frac{\xi^{-\frac{13}{6}}}{9(z^*)^{\frac{4}{3}}} \left[\Gamma\left(\frac{1}{3}, \xi^{-4} z^*\right) - \Gamma\left(\frac{1}{3}, \xi^{\frac{1}{2}} z^*\right) \right]}_{\mathcal{I}_2} \right\} d\xi, \end{aligned}$$

with Γ the upper incomplete gamma function. Integrating \mathcal{I}_1 with respect to ξ yields

$$\mathcal{I}_1 = \left[\frac{\Gamma\left(\frac{5}{8}, z^* x^{-4}\right)}{12(z^*)^{\frac{13}{8}}} \right]_1^{\frac{f_N}{f_c}} - \left[\frac{z^*}{3} \text{Ei}\left(-z^* x^{\frac{1}{2}}\right) + \frac{e^{-z^* x^{\frac{1}{2}}}(z^* x^{\frac{1}{2}} - 1)}{3z^* x} \right]_1^{\frac{f_N}{f_c}} \approx \frac{\Gamma\left(\frac{5}{8}\right)}{12(z^*)^{\frac{13}{8}}}$$

with Ei the exponential integral and the final expression is the leading-order approximation in the limits $f_N/f_c \gg 1$, $z^* \gg 1$ and $z^*(f_c/f_N)^4 \ll 1$. In the same limits, $\mathcal{I}_2 \approx \frac{2}{21} \Gamma(5/8)(z^*)^{-13/8}$, such that adding the leading-order approximations for \mathcal{I}_1 and \mathcal{I}_2 yields equation (3.8). Equation (3.8) is valid for roughly all simulation parameters and $(z - z_i) \in [0.01, 10]$.

REFERENCES

- ALEXANDER, M. J., GELLER, M., MCLANDRESS, C., POLAVARAPU, S., PREUSSE, P., SASSI, F., SATO, K., ECKERMAN, S., ERN, M., HERTZOG, A., KAWATANI, Y., PULIDO, M., SHAW, T. A., SIGMOND, M., VINCENT, R. & WATANABE, S. 2010 Recent developments in gravity-wave effects in climate models and the global distribution of gravity-wave momentum flux from observations and models. *Quarterly Journal of the Royal Meteorological Society* **136** (650), 1103–1124.
- ANSONG, J. K. & SUTHERLAND, B. R. 2010 Internal gravity waves generated by convective plumes. *Journal of Fluid Mechanics* **648**, 405.

- BORDES, G., VENAILLE, A., JOUBAUD, S., ODIER, P. & DAUXOIS, T. 2012 Experimental observation of a strong mean flow induced by internal gravity waves. *Physics of Fluids* **24** (8), 086602.
- VAN DEN BREMER, T. S. & SUTHERLAND, B. R. 2018 The wave-induced flow of internal gravity wavepackets with arbitrary aspect ratio. *Journal of Fluid Mechanics* **834**, 385408.
- BURNS, K. J., VASIL, G. M., OISHI, J. S., LECOANET, D., BROWN, B. P. & QUATAERT, E. 2018 Dedalus: A Flexible Pseudo-Spectral Framework for Solving PDEs.
- CANET, L., ROSSETTO, V., WSCHEBOR, N. & BALARAC, G. 2017 Spatiotemporal velocity-velocity correlation function in fully developed turbulence. *Phys. Rev. E* **95**, 023107.
- CARRUTHERS, D. J. & HUNT, J. C. R. 1986 Velocity fluctuations near an interface between a turbulent region and a stably stratified layer. *Journal of Fluid Mechanics* **165**, 475501.
- CHEN, S. & KRAICHNAN, R. H. 1989 Sweeping decorrelation in isotropic turbulence. *Physics of Fluids A: Fluid Dynamics* **1** (12), 2019–2024.
- CHEVILLARD, L., ROUX, S. G., LÉVÊQUE, E., MORDANT, N., PINTON, J.-F. & ARNÉODO, A. 2005 Intermittency of velocity time increments in turbulence. *Phys. Rev. Lett.* **95**, 064501.
- COUSTON, L.-A., LECOANET, D., FAVIER, B. & LE BARS, M. 2017 Dynamics of mixed convective–stably-stratified fluids. *Phys. Rev. Fluids* **2**, 094804.
- COUSTON, L.-A., LECOANET, D., FAVIER, B. & LE BARS, M. 2018 Order out of chaos: Slowly reversing mean flows emerge from turbulently generated internal waves. *Phys. Rev. Lett.* **120**, 244505.
- FAVIER, B., GODEFERD, F. S. & CAMBON, C. 2010 On space and time correlations of isotropic and rotating turbulence. *Physics of Fluids* **22** (1), 015101.
- GARAUD, P. 2018 Double-diffusive convection at low prandtl number. *Annual Review of Fluid Mechanics* **50** (1), 275–298.
- GOLDREICH, P. & KUMAR, P. 1990 Wave generation by turbulent convection. *The Astrophysical Journal* **363**, 694.
- GRISOUARD, N. & BÜHLER, O. 2012 Forcing of oceanic mean flows by dissipating internal tides. *Journal of Fluid Mechanics* **708**, 250278.
- KUNZE, E. 2017 Internal-wave-driven mixing: Global geography and budgets. *Journal of Physical Oceanography* **47** (6), 1325–1345.
- LECOANET, D., LE BARS, M., BURNS, K. J., VASIL, G. M., BROWN, B. P., QUATAERT, E. & OISHI, J. S. 2015 Numerical simulations of internal wave generation by convection in water. *Physical Review E - Statistical, Nonlinear, and Soft Matter Physics* **91** (6), 063016.
- LECOANET, D. & QUATAERT, E. 2013 Internal gravity wave excitation by turbulent convection. *Monthly Notices of the Royal Astronomical Society* **430** (3), 2363–2376.
- LIOT, O., SEYCHELLES, F., ZONTA, F., CHIBBARO, S., COUDARCHET, T., GASTEUIL, Y., PINTON, J.-F., SALORT, J. & CHILLÀ, F. 2016 Simultaneous temperature and velocity lagrangian measurements in turbulent thermal convection. *Journal of Fluid Mechanics* **794**, 655675.
- MUNROE, J. R. & SUTHERLAND, B. R. 2014 Internal wave energy radiated from a turbulent mixed layer. *Physics of Fluids* **26** (9), 096604.
- PINÇON, C., BELKACEM, K. & GOUPIL, M. J. 2016 Generation of internal gravity waves by penetrative convection. *Astronomy & Astrophysics* **588** (A122), 1—21.
- ROGERS, T. M., LIN, D. N. C. & LAU, H. H. B. 2012 Internal Gravity Waves Modulate the Apparent Misalignment of Exoplanets Around Hot Stars. *The Astrophysical Journal Letters* **758** (1), L6.
- ROGERS, T. M., LIN, D. N. C., McELWAIN, J. N. & LAU, H. H. B. 2013 Internal gravity waves in massive stars: Angular momentum transport. *The Astrophysical Journal* **772** (1).
- SANO, M., WU, X. Z. & LIBCHABER, A. 1989 Turbulence in helium-gas free convection. *Phys. Rev. A* **40**, 6421–6430.
- STAQUET, C., & SOMMERIA, J. 2002 Internal gravity waves: From instabilities to turbulence. *Annual Review of Fluid Mechanics* **34** (1), 559–593.
- TAYLOR, J. R. & SARKAR, S. 2007 Internal gravity waves generated by a turbulent bottom ekman layer. *Journal of Fluid Mechanics* **590**, 331354.
- TENNEKES, H. 1975 Eulerian and lagrangian time microscales in isotropic turbulence. *Journal of Fluid Mechanics* **67** (3), 561567.

- THORPE, S. A. 2018 Models of energy loss from internal waves breaking in the ocean. *Journal of Fluid Mechanics* **836**, 72116.
- ZHOU, Y. & RUBINSTEIN, R. 1996 Sweeping and straining effects in sound generation by high reynolds number isotropic turbulence. *Physics of Fluids* **8** (3), 647–649.